J Mater Sci (2009) 44:1664–1675
DOI 10.1007/s10853-008-3215-8

Environmental stability of the YSZ layer and the YSZ/TGO interface of an in-service EB-PVD coated high-pressure turbine blade

Wolfgang Braue

Received: 20 June 2008 / Accepted: 22 December 2008 / Published online: 22 January 2009

Abstract Hot corrosion of an in-service EB-PVD coated 1st stage high-pressure turbine (HPT) blade following an interactive $CaSO_4$ infiltration/CMAS deposition process has produced reactive interfaces with the yttria stabilized zirconia (YSZ) top coat and the TGO layer which were investigated by analytical scanning and transmission electron microscopy (TEM). Despite complete $CaSO_4$ infiltration of the coating macroscopic damage of the airfoil was confined to the pressure surface close to the trailing edge. Since the bulk composition of the $CaSO_4$/CMAS deposits exhibited a high lime-to-silica ratio $CaSO_4$/CMAS/YSZ interfaces typically involved a Ca–Zr-rich layer followed by fine-grained Ca-FSZ particles enveloping rounded YSZ column tips. No interfacial reaction was observed between the YSZ column walls and the $CaSO_4$ pore fillings. Possible terms for the formation of this unique $CaSO_4$/CMAS microstructure are evaluated. Zirconia destabilization upon hot corrosion is discussed in the light of phase compatibilities in the systems CaO–Y_2O_3–ZrO_2 and CaO–ZrO_2–SiO_2 and put into perspective with previous work on both, natural and synthetic hot corrosion deposits.

Introduction

In-flight hot corrosion of engine hardware protected by thermal barrier coatings (TBCs) may impose limitations on engine performance thus defining a serious concern of the operating airlines in terms of overall cost per flight hour [1–3]. Particularly the blades and vanes of the 1st stage of the high-pressure turbine (HPT) are closely monitored during maintenance, repair and overhaul cycles as their surfaces are directly exposed to the corrosive combustion atmosphere as well as the deposition of external airborne particles carried by the hot gas stream.

While combustion residues and high water vapor partial pressures are more a concern for all-oxide ceramic matrix composites than for zirconia-based TBCs [4], gaseous fuel contaminants, mainly SO_3, V_2O_5, and P_2O_5, are critical. Their detrimental effects on the structural integrity of yttria stabilized zirconia (YSZ)-based TBC systems have been intensively studied [5–9] and are well understood. Due to the extraction of zirconia stabilizers (e.g., MgO, CaO, Y_2O_3, CeO_2) to form sulfates, vanadates, and phosphates the t′-ZrO_2 phase is destabilized thus enhancing the deleterious transformation to m-ZrO_2 which is likely followed by TBC spallation. Rather than TBC degradation Leyens et al. [10] have identified hot corrosion of the bond coat to be even more critical as voluminous non-protective oxide scales were formed upon sodium sulfate attack.

The particles impinged on airfoil surfaces include mineral debris, sand dust, salt aerosols, and volcanic ashes ingested by the engines from the runway, during the different stages of flight operations and/or extreme weather conditions. Plugging of cooling passages has frequently been observed and erosion of leading edges is another concern [11, 12].

The early studies on uptake of hot corrosion deposits were focused on the classification of the large variety of deposits retrieved in terms of chemical and mineralogical composition and most importantly, their corresponding melting temperatures. A failure analysis of helicopter turbine engines operating in the Middle East [13] compared

W. Braue (✉)
German Aerospace Center (DLR), Materials Research Institute, Linder Hoehe, 51147 Cologne, Germany
e-mail: wolfgang.braue@dlr.de

impacted particles from cooling passages and vane surfaces with selected Ca-rich sands collected from geological sites in the actual operational areas. A good correlation between the deposits and the reference materials was established deriving a mutual melting temperature of 1,135 °C. A similar temperature range was accomplished by bulk compositions equivalent to the low melting eutectics in the quaternary CaO–MgO–Al_2O_3–SiO_2 (CMAS) system [14, 15] which proved in model infiltration experiments to be an adequate approximation for the long list of rock-forming minerals involved in hot corrosion of engine hardware.

In terms of coated airfoils, the residence time of molten salt and silicate particles may be sufficiently high to infiltrate the intercolumnar pores of EB-PVD TBCs thus degrading the compliance and strain tolerance of the top coat. Kraemer et al. [14] have demonstrated that CMAS infiltration is a fast process penetrating a 200 μm YSZ coating at less than 4 h at 1,300 °C. TBC spallation upon molten particle infiltration is considered a potential failure mode of EB-PVD TBC systems [16] which may have an impact on TBC lifetime.

Apart from model infiltration experiments few detailed informations exist in the open literature on infiltration of actual EB-PVD coated engine hardware. Siry et al. [1] referred to partial infiltration of the YSZ on a HPT airfoil by some unspecified silicate and Strangman [17, 18] reported a molten salt wicking into the YSZ layer upon a burner rig test at 875 °C/1,285 h. Although sulfate deposits are considered more a concern for rotorcraft engines operating at low altitudes [11], $CaSO_4$ deposits were reported from jet engines as well [19]. As a general rule, uptake of salt and silicate deposits represents a cumulative effect during engine service time, independent of a specific geographic location.

As a synopsis of mutual physical and chemical interaction of YSZ coatings with CMAS-type particles a schematic failure map including four regimes (infant mortality, particle erosion, infiltration of molten particles, and long-term effects, e.g., sintering of the YSZ coating, bond coat oxidation) has been proposed as a function of the TBC surface temperature and service time [20]. Although these data were primarily derived for APS-TBCs they emphasize that CMAS infiltration may be significant in the $\times$100 to $\times$1,000 h lifetime range.

Microstructural analysis of actual engine hardware offers a welcome opportunity to review and update the current understanding of hot corrosion on EB-PVD TBC systems. An in-service EB-PVD coated 1st stage HPT airfoil was chosen for this purpose. It had been retained prior to macroscopic failure thus allowing access to the full thickness of the YSZ coating. This approach is considered advantageous over fractography of damaged hardware which may already miss important constituents.

In the present case study, the infiltration/hot corrosion process investigated combines the simultaneous effects of both, a salt-type ($CaSO_4$) and a CMAS-type silicate deposit arranged in a layered microstructure with $CaSO_4$ forming the base of the deposits in most cases. Notably the YSZ coating was *completely* infiltrated with $CaSO_4$ prior to deposition of CMAS. It is with respect to this unique feature that this study differs from previous work [13, 19, 21, 22], which refers to $CaSO_4$ as a surface deposit exclusively devoid the interaction with a silicate-type hot corrosion deposit.

From this hot corrosion process reactive interfaces at the top and bottom surfaces of the coating emerged which are analyzed by scanning electron microscopy (SEM) and focused-ion-beam (FIB) assisted analytical transmission electron microscopy (TEM).

The diffusion path of $CaSO_4$/CMAS-type constituents is monitored from the corroded YSZ top coat all the way down to the TGO/bond coat interface. Despite the microstructural complexity of EB-PVD-coated airfoils the underlying reaction pattern controlling corrosive attack and partial dissolution of the YSZ coating proves to be relatively straightforward and is put into perspective with microstructures reported from similar hot corrosion deposits.

Experimental

Following optical inspection of the airfoil a detailed microstructural analysis of selected cross sections was performed in a scanning electron microscope (LEO Ultra 55, Zeiss Inc., Oberkochen, Germany) equipped with a energy-dispersive nanospectroscopy (EDS) system (Oxford Instruments, Oxfordshire, UK).

Quantification of SEM-EDS spectra was achieved through the conventional ZAF correction procedure for atomic number Z, absorption and fluorescence employing element standards.

Cross section TEM specimens from selected regions of the airfoil (Fig. 1) were prepared via FIB sectioning through the lift-out technique employing a single source FIB (Strata 205, FEI Inc., Eindhoven, The Netherlands).

A 300 kV Tecnai F30 transmission electron microscope (FEI Inc.) with a field emission gun was utilizing for nanoscale analysis of selected FIB lamellae. Besides conventional TEM work dark-field imaging in scanning transmission (STEM) mode employing a high-angle annular dark field (HAADF) detector was used for Z-contrast imaging in conjunction with EDS, selected area diffraction (SAD), and convergent-beam electron diffraction (CBED). Electron diffraction patterns are printed with inverse contrast.

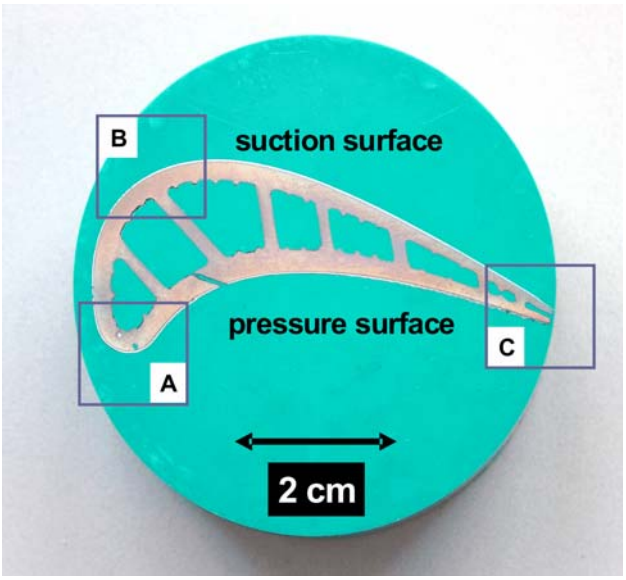

Fig. 1 Cross-sectional optical micrograph of HPT airfoil displaying the regions of interest: (i) leading edge (region A), (ii) hot spot on the suction-surface (region B), and (iii) trailing edge (region C)

Results

General microstructure of the airfoil and hot corrosion deposits

As displayed in Fig. 2 the basic microstructure of the airfoil comprised a γ/γ' PWA 1484 Ni-base alloy, a two-phase γ-Ni/ß-NiAl LPPS-MCrAlY bond coat (thickness 80 µm) with Hf, Y and Si added [23] and a standard EB-PVD 7YSZ top coat. Thickness of the thermally grown oxide (TGO) layer was approximately 1.5 µm with numerous Hf-bearing oxide pegs at the TGO/bond coat interface, typical of reactive element doped systems. Similar materials systems are widely used in P&W 4000-type engines. The accumulated in-service time of the HPT blade was 17.000 h which is equivalent to 3,000 cycles of the engine in different operating regions [T. Fischer, Lufthansa Technik AG, private communication].

The average retained thickness of the YSZ top coat at the leading edge was of the order of 130 microns which tapered off to significant lower thicknesses (60 µm) retained at the trailing edge. Notably the intercolumnar pores of the coating and and even the thin feather arms were found to be completely infiltrated with a dense, fine-grained, secondary phase (Fig. 3a–c) identified as the orthorhombic phase anhydrite, $CaSO_4$ (JCPDS-file 6-0226, [24, 25]) by means of electron diffraction and small probe microanalysis. Deviations from the typical columnar grain structure of the YSZ in Figs. 2 and 3 are due to non-planar sectioning of the airfoil. Figure 4 displays a STEM dark-field image from the YSZ/TGO interface at the leading

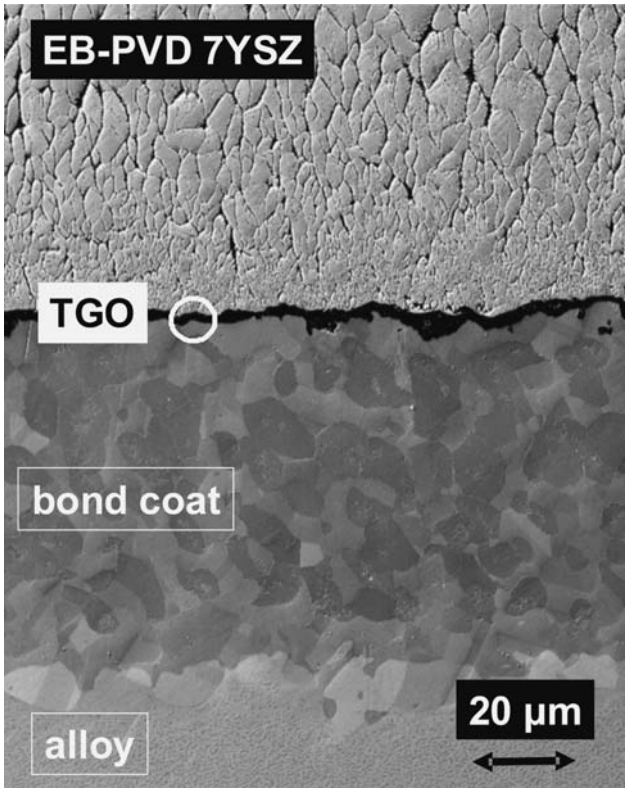

Fig. 2 The general microstructure of the HPT blade studied: a PWA 1484-type base alloy, a two-phase LPPS-MCrAlY bond coat, the thermally grown oxide (TGO) layer and a standard EB-PVD 7 YSZ top coat (SEM, secondary electron image)

edge emphasizing that the $CaSO_4$ fillings extended indeed through the full thickness of the coating. EDS analysis showed that anhydrite composition was stoichiometric with neither dissolved impurities nor Y or Zr from the coating. No evidence for a reaction zone between the $CaSO_4$ and the column walls was obtained (see also the section "The $CaSO_4$/YSZ- and CMAS/YSZ interfacial reaction zones"). These prominent features were observed at all airfoil locations exhibiting an intact YSZ top coat.

Original CMAS-type hot corrosion deposits sticking to the airfoil could only be retrieved from the pressure surface except for a small section right at the trailing edge shown in Fig. 5. Complete loss of the YSZ coating and severe attack of the TGO layer and the bond coat were evident in this area. A few millimeters off the trailing edge the YSZ coating had hot corrosion deposits still intact. The deposit from the boxed region in Fig. 5 exhibited a droplet-type morphology (Fig. 6), typically 300 × 50 microns with $CaSO_4$ pore fillings extending through the full YSZ thickness. Microstructural analysis confirmed that the deposit was completely crystalline. Most CMAS deposits appeared as if floating on a discontinuous $CaSO_4$ layer which obviously represented the sulfate surplus after infiltration of the YSZ top coat has been completed.

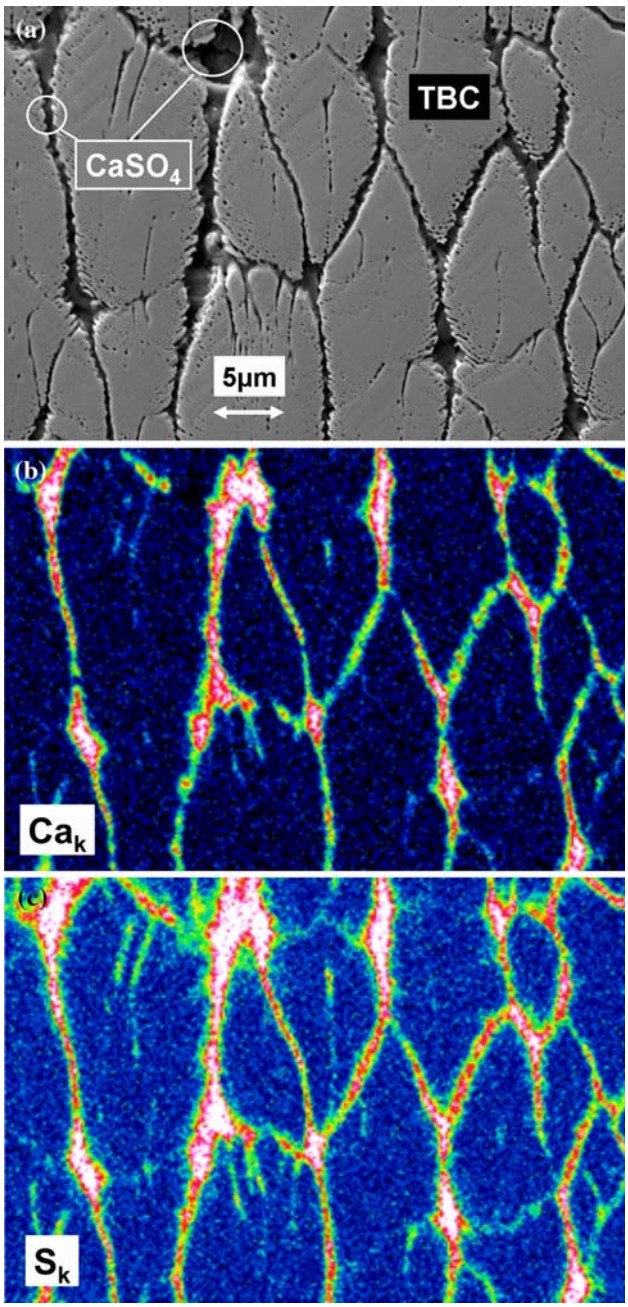

Fig. 3 **a** middle section of the YSZ top coat displaying $CaSO_4$ infiltration of open porosity (suction-surface/region B, SEM, secondary electron image), **b** and **c** elementary mapping (Ca_k, S_k) proving that $CaSO_4$ is continuous within the intercolumnar pore network of the coating

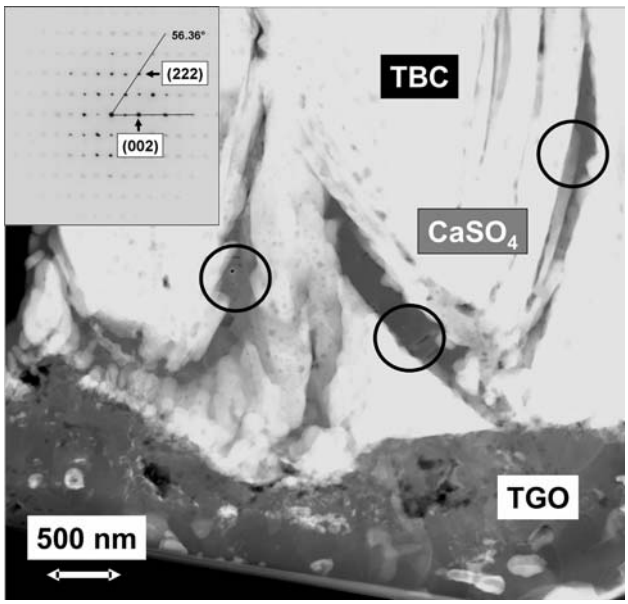

Fig. 4 Intercolumnar anhydrite fillings from the YSZ root section extending into the upper TGO layer (leading edge/region A, STEM HAADF image). Note high defect density (pores, microcracks) in the TGO. Inset shows selected area diffraction (SAD) pattern of anhydrite $CaSO_4$ oriented parallel to B = $[\bar{1}10]$

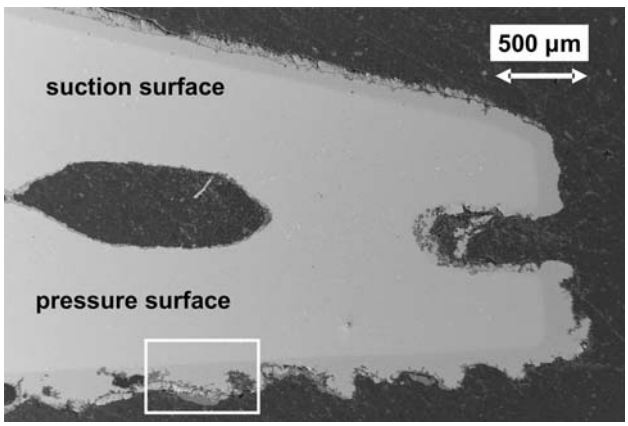

Fig. 5 Loss of coating and bond coat oxidation along the pressure surface close to the trailing edge/region C (SEM, secondary electron image). Eventually the coating recovers with CMAS-type deposits still attached in selected locations (see Fig. 6 for boxed region at high magnification)

The bulk composition of the CMAS droplet has been determined from EDS area analysis and is compiled in Table 1. The lime-to-silica ratio is higher (1.5 vs. 0.7) as compared to silica-saturated synthetic CMAS compositions [14]. Minor constituents such as TiO_2, NiO, and notably FeO stem from uptake of metallic compounds. Moreover, SO_3 and P_2O_5 could be identified unambiguously in small quantities. The detection of Zr indicated dissolution of t′-ZrO_2 grains and Zr uptake by the original CMAS melt. Most likely Y was also involved in the dissolution process, but the actual yttria uptake was probably below the EDS detection limit.

The CMAS bulk composition is conveniently displayed in the 10 wt% MgO plane of the quaternary CMAS [26] where it plots on the cotectic line between the primary fields of cyrstallization of melilite Ca_2 (Al, Fe, Mg) (Si, Al)$_2O_7$ and spinel (Mg,Fe)Al_2O_4. From this phase diagram a liquidus temperature of 1,400 °C is a realistic measure

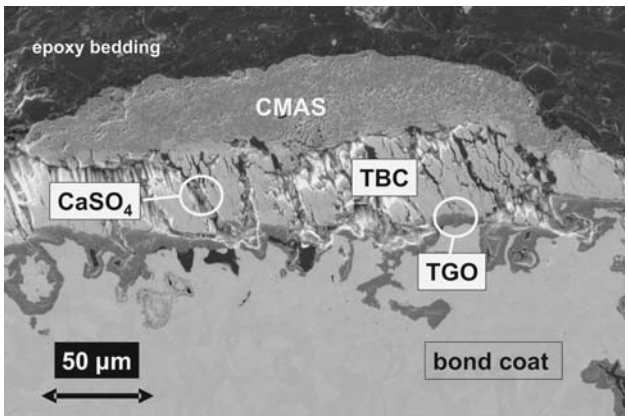

Fig. 6 CMAS-type hot corrosion deposit adhering to the YSZ top coat (boxed region from Fig. 5). Note $CaSO_4$ pore fillings of the top coat (trailing edge/region C, SEM, secondary electron image)

Table 1 Chemical composition of CMAS-type deposit from this study as compared to a synthetic CMAS composition [14]

	CMAS (this study)	CMAS (from [14])
Oxide (wt%)		
CaO	33.6	33.2
MgO	9.9	6.5
Al_2O_3	10.1	11.8
SiO_2	22.4	48.5
TiO_2	3.0	
FeO	15.4	
NiO	0.8	
SO_3	3.2	
P_2O_5	0.7	
ZrO_2	0.9	

which is expected to drop significantly when the effects of Fe and the high water vapor partial pressure in the combustion gases are taken into account. TEM revealed a two-phase CMAS microstructure comprising a Mg–Al-bearing phase (presumably spinel) embedded in a crystalline Ca–Al–Si-rich matrix phase. Additional Ca-rich phases including perovskite $CaTiO_3$ and wollastonite $CaSiO_3$ were abundant. The lower CMAS section facing the YSZ coating was rather dense while considerable porosity developed in the upper section.

The $CaSO_4$/YSZ- and CMAS/YSZ interfacial reaction zones

Interfacial reactions of the YSZ top coat with the $CaSO_4$ and the CMAS deposits resulted in partial dissolution of zirconia and produced new phase assemblages. The basic reaction scheme is first shown for the $CaSO_4$/YSZ interface in a deposit exhibiting a $CaSO_4$ base underneath the CMAS deposit (Figs. 6, 7a). Due to the high purity of the sulfate the $CaSO_4$/YSZ interface exhibited a low background of minor constituents (FeO, Al_2O_3, SiO_2, and TiO_2).

As shown in the close-ups (Fig. 7 a/b) this interface involved a Ca-Zr rich phase (later identified as $CaZrO_3$, see below) followed by numerous small equiaxed Ca-rich fully stabilized zirconia (FSZ) grains enveloping rounded YSZ column tips. The CaO concentration of the FSZ grains was of the order of 12 wt%, some grains were co-stabilized with an additional 1.5% wt Y_2O_3. The YSZ tips were co-stabilized by CaO and Y_2O_3 which changed for the standard 7 YSZ composition when analyzed further away from the interface. The marked morphology change of the originally faceted column tips was interpreted as additional evidence for dissolution of the top coat during interaction with the $CaSO_4$/CMAS deposits. The Ca–Zr phase was identified as the perovskite-type $CaZrO_3$ via electron diffraction from a FIB lamella across the $CaSO_4$/YSZ interface. The $B = [\bar{1}01]$ zone axis pattern is shown in Fig. 7c and is indexed according to the orthorhombic $CaZrO_3$ cell as listed in the JCPDS-file 35-0790, [24].

Due to the complex CMAS composition (Table 1) CMAS/YSZ interfaces usually featured a higher background of minor constituents (FeO, Al_2O_3, SiO_2, and TiO_2) as compared to $CaSO_4$/CMAS interfaces. The perovskite phase $CaZrO_3$ is well-known for its limited homogeneity range [27, 28]. Thus the pure $CaZrO_3$ phase was not stable at the CMAS/YSZ interface and different phase relationships involving an Al-bearing Ca–Zr–Fe-silicate phase prevailed instead. The CMAS/YSZ interface is displayed in Fig. 8 in backscattered electron mode with the Ca–Zr–Fe-silicate layer standing out as a very prominent feature even at low magnification. Except for the occurrence of the Ca–Zr–Fe-silicate phase the microstructures of the CMAS/YSZ and the $CaSO_4$/YSZ reaction zones were very similar. This is particularly true for the rounded YSZ tips of the retained coating. For both cases, the average total thickness of the reaction zone was of the order of 5 µm.

A more detailed insight into the phase assemblage of the CMAS/YSZ reaction zone was provided by FIB assisted analytical TEM and electron diffraction as compiled in Fig. 9a–c. Right at the interface the Al_2O_3, FeO, and SiO_2 concentrations dissolved in the Ca–Zr–Fe-silicate were rather low while several microns off the interface considerable amounts of SiO_2, Al_2O_3, and particularly FeO ($\geq$10 wt%) were achieved. The yttria content was of the order of 3 wt%. The experimental zone axis pattern of the Ca–Zr–Fe-silicate as shown in Fig. 9b could be matched to the orthorhombic phase $Ca_2ZrSi_4O_{12}$ [29] oriented parallel to $B = [001]$ which obviously can accommodate a large homogeneity range than given by the strictly ternary composition (see "Discussion" section). Electron diffraction patterns obtained from the Ca-silicate coexisting with

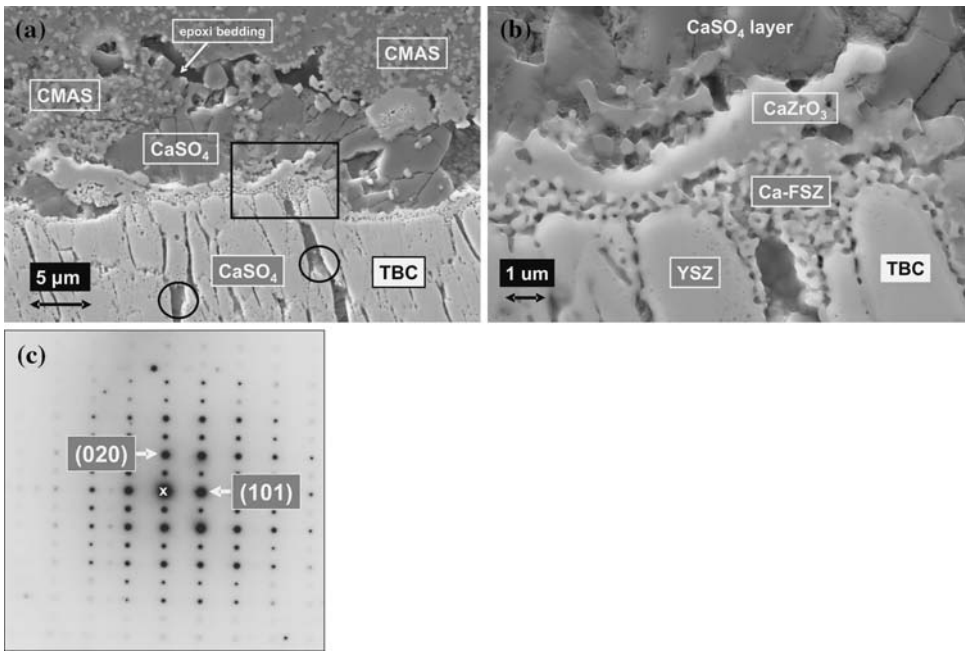

Fig. 7 **a** $CaSO_4$/YSZ reaction zone from a deposit exhibiting a distinct $CaSO_4$ base underneath the actual CMAS part. See **b** for boxed region (trailing edge/region C, SEM, secondary electron image). **b** Interfacial reaction between the $CaSO_4$ base of hot corrosion deposit (**a**) and the YSZ top coat introducing a $CaZrO_3$ layer and small Ca-FSZ particles enveloping rounded YSZ column tips (trailing edge/region C, SEM, secondary electron image). **c** Zone axis pattern obtained from $CaZrO_3$ layer at the $CaSO_4$/YSZ interface. Indexing is consistent with the orthorhombic cell (JCPDS-file 35-0790, [24]). Orientation is parallel to $B = [\bar{1}01]$

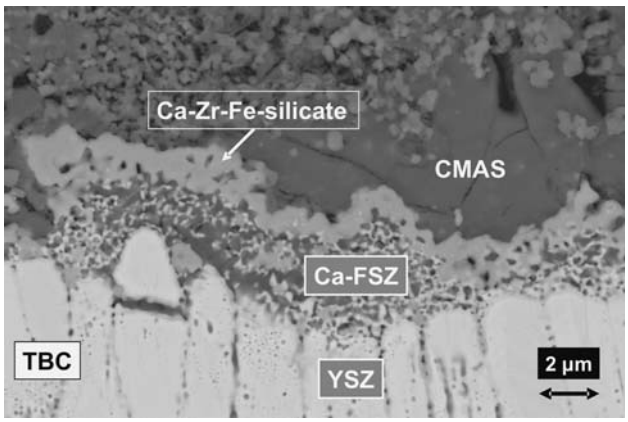

Fig. 8 CMAS/YSZ reaction zone comprising a Ca–Zr–Fe-silicate layer, fine-grained Ca-FSZ particles and YSZ. Note the rounded column tips of the top coat (trailing edge/region C, SEM, back-scattered electron image)

the Ca–Zr–Fe-silicate were consistent with the triclinic cell [30] of wollastonite, $CaSiO_3$ (Fig. 10c). The Ca–Zr–Fe-silicate phase incorporated a number of nanoscale FSZ particles, very similar to the interfaces displayed in Figs. 7b and 8.

Usually the $CaSO_4$/YSZ- and CMAS/YSZ reaction zones sustained their flat layered microstructure with respect to the original coating surface and did not penetrate far into the intercolumnar pore network. An exception to this rule is displayed in Fig. 10. Owing to the fact that a bulge in the bond coat (see inset in Fig. 10) had created sufficient tensile stresses in the coating CMAS and reaction products from the CMAS/YSZ interface could penetrate the now enlarged pores.

The YSZ/TGO interface upon interdiffusion of $CaSO_4$/CMAS constituents

Since the YSZ coating of the airfoil was intact apart from the trailing edge (Fig. 3), no direct CMAS/TGO interfaces were accessible. The typical phase assemblage of the TGO layer consisted of α-alumina and (Ni, Co)Cr_2O_4 spinel grains as indicated by the high Ti, Cr, Co, and Ni concentrations inn the EDS spectra. However, interdiffusion of $CaSO_4$- and CMAS constituents including Na (traces only), Mg, Ca, and S via the intercolumnar pore network of the coating to the upper TGO layer introduced a distinct reaction zone (thickness $\leq$ 1 µm) between the columnar alumina zone (CAZ) and the YSZ root section, as shown in Fig. 11a. Here the average SO_3 concentration was of the order of 4 wt%. Those sections of the reaction zone in direct contact with $CaSO_4$ pore fillings (see left part of Fig. 11a) were rather dense holding perovskite $CaTiO_3$ and some spinel $MgAl_2O_4$. Calcium was still enriched in the more porous fine-grained sections of the reaction zone (see right part of Fig. 11a) featuring similarities with the alumina-zirconia intermixed zone typical of MCrAlY-based TGO layers [31].

Element profiling across YSZ roots sections (Fig. 11a) revealed a Ca-and Ti-enrichment (1.7 vs. 1.4 wt%, respectively) within a narrow zone of approximately 1 µm thickness. The corresponding yttria content was of the order of 4 wt % which increased to the nominal 7 YSZ composition with increasing distance from the YSZ/TGO interface. Notably Ca, Ti, Ni, and even S prevailed in small concentrations further up within the YSZ columns. As compared to the upper YSZ columns the enrichment zone

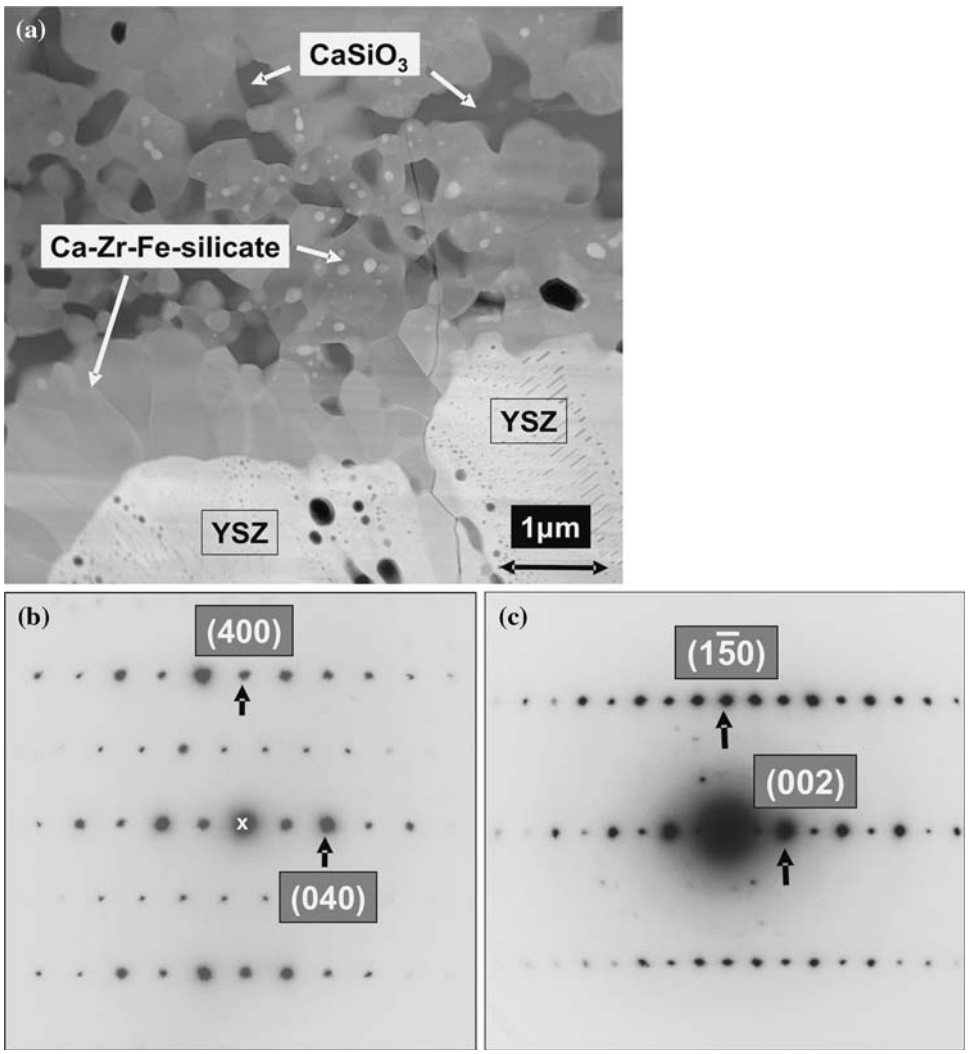

Fig. 9 **a** Ca–Zr–Fe-silicate phase (with intragranular zirconia grains) and wollastonite $CaSiO_3$ from the CMAS/YSZ reaction zone in contact with rounded YSZ tips (trailing edge/region C, STEM HAADF image). **b** Zone axis orientation pattern obtained from the Ca–Zr–Fe-silicate coexisting with wollastonite at the CMAS/YSZ interface. Indexing is consistent with the orthorhomic phase $Ca_2ZrSi_4O_{12}$ [29] oriented parallel to $B = [001]$. **c** Zone axis orientation pattern obtained from Ca-silicate from the CMAS/YSZ reaction zone. Indexing is consistent with the triclinic cell [30] of wollastonite $CaSiO_3$ with $B = [\bar{5}10]$

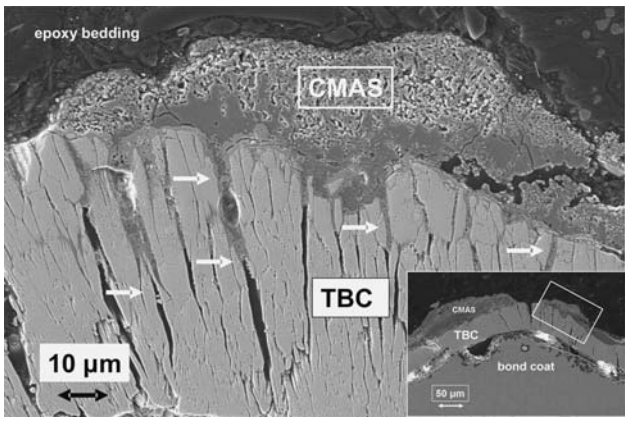

Fig. 10 Reaction products from the CMAS/YSZ interface filling the larger pores of the YSZ top coat (see arrows) after a bulge of the bond coat (see inset) has created sufficient tensile stresses in the coating (trailing edge/region C, SEM, secondary electron image)

in the root section had a slightly different secondary electron coefficient and appeared more dense. Apart from hafnia-rich pegs the CAZ consisted of pure α-alumina devoid of dissolved impurities or $CaSO_4$/CMAS constituents.

As highlighted in Fig. 11b, the Ca- and Mg enriched phase in the upper TGO layer dissolved the YSZ root section via grain boundary attack introducing deep fissures into the coating which left individual zirconia grains behind the reaction front. Small probe microanalysis of these zirconia particles indicated co-stabilization by Ca and Y, but quantification of the EDS spectra was ambiguous due to the high Ca background from other phases.

The TGO/bond coat interface upon interdiffusion of $CaSO_4$/CMAS constituents

While most sections of the TGO layer appeared dense and homogeneous, some regions revealed a high defect density characterized by clustered porosity and numerous microcracks as displayed in Fig. 4 for the leading edge. These microcracks in the TGO layer provided a convenient path for further diffusion of $CaSO_4$/CMAS constituents through

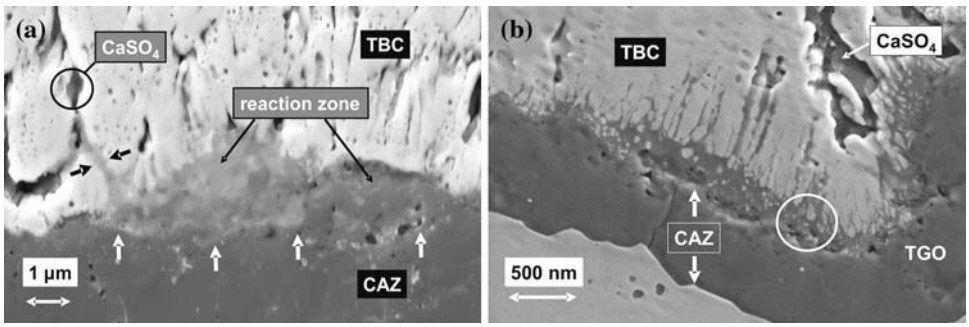

Fig. 11 **a** Reaction zone between interdiffused $CaSO_4$/CMAS constituents (e.g., Na, Mg, Ca, S) and the upper TGO layer just above the columnar alumina zone (CAZ). The upper CAZ boundary is highlighted by arrows (trailing edge/region C, SEM, secondary electron image). **b** Partial dissolution/fragmentation of the YSZ root section by a Mg-and Ca-enriched phase in the upper TGO layer leaving several large zirconia grains (highlighted in circled region) behind the reaction front (suction side/region B, SEM, secondary electron image, CAZ: columnar alumina zone)

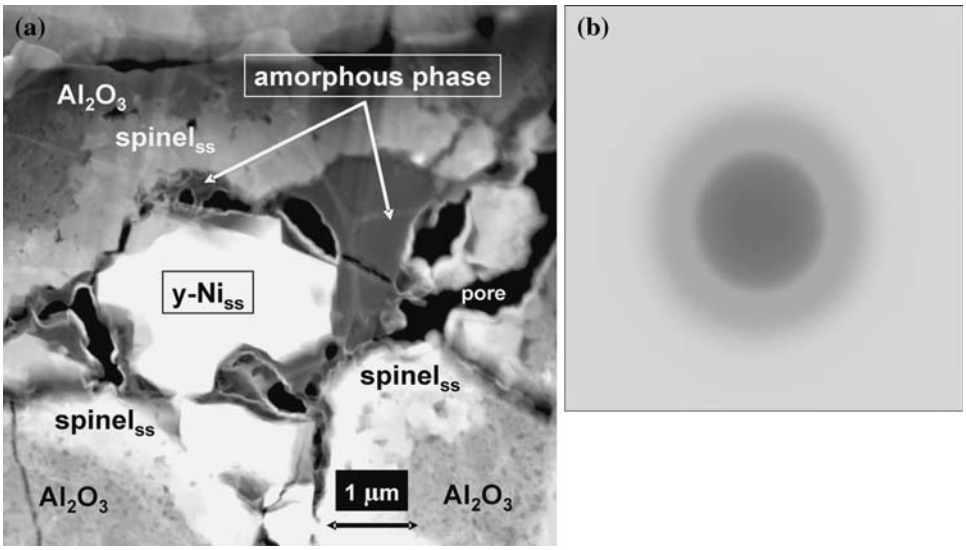

Fig. 12 **a** Amorphous phase pockets (dark gray contrast) next to a γ-Ni_{ss} grain and spinel particles of varying composition from a porous/cracked section of the TGO layer at the TGO/bond coat interface (leading edge/region A, STEM HAADF image). The alumina-rich amorphous phase holds substantial amounts of Na, K, Mg, Al, S, Ca, and Y. **b** Convergent-beam electron diffraction (CBED) pattern proving the amorphous nature of impurity-rich pocket displayed in **a**

the TGO layer to the TGO/bond coat interface. FIB sectioning of a similar TGO area (Fig. 12a) revealed pockets of an alumina-rich amorphous phase adjacent to a γ-Ni grain enveloped by $NiAl_2O_4$- and/or low-alumina $Co(Cr, Al)_2O_4$ spinel particles. The amorphous phase provided a sink for considerable amounts of Mg, Ca, S, P, Cl, and Y along with minor amounts of metal constituents (Ti, Fe, Cr, Co, Ni,), as shown by x-ray microanalysis. Confirmation of Na is difficult because of a peak coincidence with Ga introduced during FIB sectioning.

The amorphous nature of these pockets was unambiguously verified by CBED as shown in Fig. 12b. On a gross scale segregation of alkalis-, alkaline earths, and sulfur (among other elements) to this amorphous phase mark the end of a pronounced diffusion path for $CaSO_4$/CMAS constituents which started out at the $CaSO_4$/CMAS/YSZ interfaces and could be monitored all the way down to the TGO/bond coat interface in selected TGO regions.

Discussion

The common observation [11, 32, 33] that airfoil surfaces, particularly the leading edge and the pressure side, can aerodynamically capture CMAS-type particles may furnish an appropriate explanation for the prevalent occurrence of CMAS-type deposits on the pressure side of the airfoil from this study. The reduced thickness of the TBC coating at the trailing edge (Fig. 5) and insufficient cooling may have enabled higher surface temperatures than in other locations of the airfoil resulting in local overheating and melting of adhering hot corrosion deposits.

The layered microstructure of most CMAS deposits exhibiting a $CaSO_4$ base (Fig. 7a) implies that CMAS was deposited at the YSZ surface some time after infiltration of the coating has been completed. The interpretations offered for $CaSO_4$ formation in the literature including (i) ingestion of gypsum $CaSO_4 \cdot 2H_20$ as mineral dust [22], (ii) a

calcium carbonate reaction with sulfur contaminants in the fuel [13], and (iii) sulfidation of Ca_2SiO_4 from the CMAS [34] are well suited to explain a $CaSO_4$ *surface* deposit, but fail to rationalize complete infiltration of the intercolumnar pore network given the high melting point of anhydrite $CaSO_4$ (1,450 °C).

Considering the low ternary eutectic (738 °C) in the ternary system $CaSO_4$–$MgSO_4$–Na_2SO_4 [35] an originally ternary salt mixture which became enriched in $CaSO_4$ upon volatilization of Na_2SO_4 and $MgSO_4$ appears a likely proposition. But this mechanism probably requires considerable residence time. Alternatively, condensation of a $CaSO_4$ rich vapor phase on the internally cooled airfoil would provide a fast and efficient mechanism for YSZ infiltration due to the very small grain sizes involved. The high purity of the $CaSO_4$ pore fillings and their homogeneous distribution across the full thickness of the YSZ coating support this argument. But open questions prevail since particle impingement is considered more likely for salt deposits than equilibrium condensation from the vapor phase [8, 33]. Just like Na_2SO_4 [36], the dew point of $CaSO_4$ at the blade is expected to be a complex function of the sulfur content in the fuel, the salt concentration and the true surface temperatures of the airfoil. Since these data are currently not available, the issue of $CaSO_4$ formation is left to forthcoming research.

It should be noted however that the high water partial pressures in the combustion gases could very effectively reduce melting temperatures. Interestingly the conception that sulfates within the $CaSO_4$/CMAS deposits became molten first and started to preferentially wick into the YSZ coating before the CMAS became molten complies with microanalytical data obtained from actual engine hardware [T. Strangman, Honeywell, personal communication]. On the other hand water vapor induced corrosive attack of Al- and Si bearing compounds from CMAS deposits may cause an increase of the TBC surface temperature due to evaporation of $Al(OH)_3$ and $Si(OH)_4$ [11], but this effect is probably less critical.

The fact that $CaSO_4$ can coexist with CMAS in one deposit raises the question of miscibility between sulfate and silicate melts providing $CaSO_4$ has gone indeed through the molten state. This issue has been addressed by experimental work in clinker cement systems. For the CaO–Al_2O_3–Fe_2O_3–SiO_2–$CaSO_4$–K_2SO_4 system it has been shown [37, 38] that the sulfate eutectic is exceeded at 850 °C. At 1,350 °C Al_2O_3, Fe_2O_3 und SiO_2 are comparatively insoluble in the sulfate melt and SO_4^{2-} is virtually insoluble in the oxide melt, whereas Ca, K, and Na are soluble in both liquids. Similar oxide-sulfate liquid immiscibility may contribute to the fact that $CaSO_4$ and CMAS persist without intermixing.

The combined effects of $CaSO_4$ and CMAS deposits provided a high CaO/SiO_2 ratio at the original YSZ surface which represented the key parameter controlling mutual interfacial reaction schemes. As a major result of this study the $CaSO_4$/YSZ and CMAS/YSZ eventually merged into a very similar type of interfacial reaction zone. The simplest case of a pure $CaZrO_3$ layer ($CaSO_4$/YSZ interface, Fig. 7b) followed by (Ca + Y)-FSZ grains enveloping the YSZ tips is consistent with the sequence $CaZrO_3$ → c-ZrO_2 → t-ZrO_2 in the ternary system CaO–Y_2O_3–ZrO_2 (see diagram Zr-274 in ref. [39]).

The detailed phase relationships resulting in the formation of the Al-bearing Ca–Zr–Fe-silicate phase at the CMAS/YSZ interface (Figs. 8, 9a) are currently unknown. However, previous work on phase compatibilities in the system CaO–ZrO_2–SiO_2 at 1,300 °C (see diagrams Zr-288 and Zr-289 in [39], [40] for review) may serve as a first approximation. The 1,300 °C isothermal section holds two stable ternary compounds, $Ca_2ZrSi_4O_{12}$ [29, 41] and $Ca_3ZrSi_2O_9$ [29, 42], the latter also reported as the mineral baghdadite [43]. A third compound $CaZrSi_2O_7$, known as the mineral gittinsite [44] is apparently unstable under these conditions. As shown schematically in Fig. 13, both phases, $Ca_2ZrSi_4O_{12}$ and $Ca_3ZrSi_2O_9$ can coexist with wollastonite $CaSiO_3$ and zirconia, in agreement with the

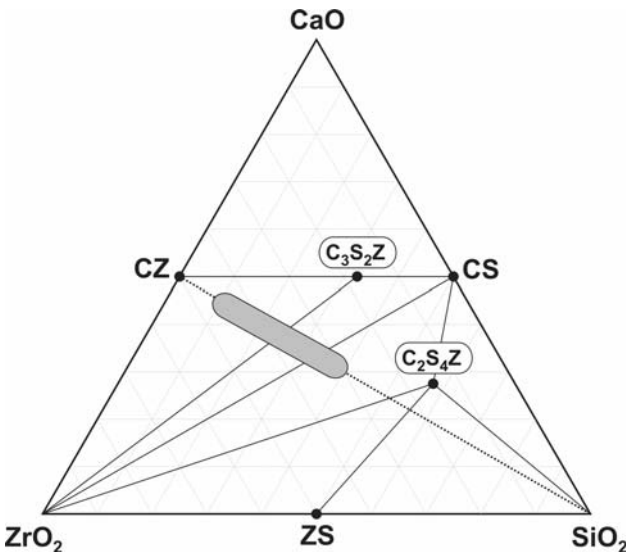

Fig. 13 Compatibility triangles in the ternary CaO–ZrO_2–SiO_2 (mol%) at 1,300 °C (modified after [39, 40]) serving as a first approximation for pertinent phase assemblages at the CMAS/YSZ interface. Shaded area represents the compositional variation of the Ca–Zr–Fe-silicate which plots close to the join CZ-SiO_2 (given by dotted line). Abbreviations: C = CaO, S = SiO_2, Z = ZrO_2, CZ = $CaZrO_3$, C_3S_2Z = $Ca_3ZrSi_2O_9$, C_2S_4Z = $Ca_2ZrSi_4O_{12}$, CS = $CaSiO_3$, ZS = $ZrSiO_4$. Compatibility triangles in the subsystem CaO–CZ–CS are omitted

interfacial microstructure discussed in "General microstructure of the airfoil and hot corrosion deposits" section. The normalized compositions of the Ca–Zr–Fe-silicate as determined by small probe x-ray microanalysis plot close to the join $CaZrO_3$–SiO_2. Following a recent refinement of phase compatibilities involving tetragonal and cubic zirconia [40] it should be the $Ca_3ZrSi_2O_9$ phase which is compatible with either t-ZrO_{2ss} or c-ZrO_{2ss} and $CaZrO_3$ (not shown in Fig. 13 for simplification). However, the experimental electron diffraction data obtained from the Ca–Zr–Fe-silicate (Fig. 9b) could only be matched by the orthorhombic cell of the $Ca_2ZrSi_4O_{12}$ phase [29] which may be due to a larger solubility for Fe and Al. This is in line with recent work [45] on crystallization of the $Ca_2ZrSi_4O_{12}$ phase from glasses in the system CaO–Al_2O_3–ZrO_2–SiO_2 containing up to 10 mol% Al_2O_3. The role of Fe on the homogeneity range of the $Ca_2ZrSi_4O_{12}$ phase is currently unknown and has to be evaluated in forthcoming research.

The reaction between the $CaSO_4$ and the coating is very obvious at the YSZ surface but the infiltrated $CaSO_4$ did not react with the column walls of the t′-ZrO_2 phase in the coating (Fig. 4) For a synthetic CMAS system [14] a thin Y-depleted m-ZrO_2 layer was reported only from a column wall close to the CMAS/TBC surface, so the discrepancy in CMAS reactivity between the YSZ surface and the intercolumnar pores prevailed. For the airfoil a mutual argument is related to the fact that due to internal cooling and sufficient thermal insulation the effective temperatures in the coating are too low to promote a reaction between the $CaSO_4$ and the t′-ZrO_2 phase. A study employing nanocrystalline ZrO_2–$CaSO_4$ mixtures prepared by the sol-gel route [46] showed no reaction up to 800 °C and produced t-ZrO_2 and anhydrite only. CMAS infiltration may be limited with Gd-zirconate-based coatings instead of the standard 7YSZ composition due to rapid dissolution of the $Gd_2Z_2O_7$ phase and sealing of the intercolumnar gaps with the precipitated reaction products [47].

In terms of dissolution and possible reprecipitation of zirconia and yttria at the CMAS/YSZ interface the composition of the glassy phase first formed upon partial melting of the $CaSO_4$/CMAS deposits is strongly dependent on the CaO/SiO_2 ratio. In such glasses Zr can act as both, a network former as well as a network modifier, depending on the concentration of the dominant network modifier Ca [19, 21, 22]. This has been confirmed in recent spectroscopic work on CaO–ZrO_2–SiO_2 glasses [48, 49].

For a basic melt with a high CaO/SiO_2 ratio equivalent to the present study, the dissolved ZrO_2 acts as a network-forming oxide, more readily than Y_2O_3 [19, 21, 22]. Unlike an acidic melt the Zr solubility limit is not exceeded, therefore no yttria-depleted zirconia grains are reprecipitated in the YSZ reaction zone, in agreement with the present study. The overabundance of Ca at all reactive interfaces investigated promoted Ca co-stabilization of the zirconia grains thus offering no margin for the formation of m-ZrO_2 upon cooling.

Hot corrosion scenarios [14–16, 47] which featured a lower CaO/SiO_2 ratio in the CMAS composition as compared to this study generated different zirconia phase relationships at the CMAS/YSZ interface which did not allow for the formation of crystalline Ca–Zr-bearing compounds. For their synthetic CMAS system (see Table 1) Kraemer et al. [14] found Y-depleted m-ZrO_2 close to the CMAS while Y-enriched c-ZrO_2 formed at the YSZ root section. Except for these zirconia polymorphs no other Zr-or Y-bearing phase was reported.

The effects of interdiffusion of $CaSO_4$/CMAS constituents through the coating to the upper TGO layer can by monitored in (i) the occurrence of newly formed phases ($CaTiO_3$, spinel $MgAl_2O_4$, Fig. 11a), (ii) the small Ca-enrichment zone of the YSZ root section, and (iii) corrosive attack and fragmentation of the lower YSZ section along grain boundaries (Fig. 11b). Segregation of $CaSO_4$/CMAS constituents to amorphous pockets close to the TGO/bond coat interface (Fig. 12a) is clearly left to selected TGO regions exhibiting numerous microcracks and clustered porosity. Such TGO microstructures have been retrieved from the leading edge (Fig. 4). Similar Ca-rich phases have been reported from airfoils upon diffusional reaction between the TGO and hot corrosion deposits in areas of localized YSZ spallation [32]. There is still the possibility that the Y in the amorphous pockets may originate from the MCrAlY bond coat. Mendis et al. [50] reported Y-rich precipitates containing S from oxide pegs at the TGO/bond coat interface. In the present study the joint segregation of Mg and Ca and S (among others) to selected areas of the TGO layer strongly suggests interdiffusion of $CaSO_4$/CMAS constituents.

No critical hardware damage or TBC spallation has been observed for the airfoil of this study. However, it has been pointed out [11, 20] that EB-PVD TBCs can tolerate limited CMAS penetration only and the damage mechanisms associated with delaminations and separations in the infiltrated part of the coating [16] clearly identify CMAS infiltration as a potential threat for TBC life. Siry et al. [1] considered the enhanced sintering of zirconia upon infiltration even more critical than intrinsic hot corrosion effects. Efficient air inlet filtration and an additional sputtered YSZ top coat including dense electrically biased layers has proved as appropriate measures to inhibit salt or CMAS infiltration of EB-PVD TBCs [11]. Even though $CaSO_4$ infiltration may be difficult to prevent the beneficial role of $CaSO_4$ in terms of sulfur gettering must not be overlooked.

Conclusions

Hot corrosion of an in-service EB-PVD coated 1st stage HPT blade has been exploited via analytical electron microscopy. The airfoil was removed from the engine prior to macroscopic damage and/or YSZ spallation and had experienced complete $CaSO_4$ infiltration of the YSZ layer prior to deposition of CMAS-type deposits. CMAS droplets were retrieved from the pressure surface close to the trailing edge.

The reactivity of the YSZ coating upon corrosive attack was controlled by the high lime-to-silica ratio imposed by the $CaSO_4$/CMAS deposits. Upon partial dissolution of the YSZ the interfacial reaction zone at the $CaSO_4$/YSZ and CMAS/YSZ interfaces (when separated) shared very similar microstructures which only differed by the relative abundance of Al_2O_3, TiO_2, FeO, and SiO_2: namely a $CaZrO_3$ layer (alternatively a Ca–Zr–Fe-silicate, presumably the Fe-bearing $Ca_2ZrSi_4O_{12}$ phase at the CMAS/YSZ interface) followed by fine-grained Ca-FSZ particles which envelop the former faceted, now rounded YSZ column tips. The reaction zone could be rationalized by phase compatibilities in the ternary systems $CaO–Y_2O_3–ZrO_2$ and $CaO–ZrO_2–SiO_2$, respectively.

Interdiffusion of $CaSO_4$/CMAS constituent to the upper TGO layer gave rise to noticeable microstructural changes as compared to TGO's from as-coated EB-PVD TBC's. These included (i) newly formed phases ($CaTiO_3$, $MgAl_2O_4$), (ii) a small Ca-enrichment zone at the YSZ root section, and (iii) corrosive attack/fragmentation of the coating along grain boundaries. Segregation of $CaSO_4$/CMAS constituents (e.g., Mg, Ca, S) to amorphous alumina-rich pockets retrieved from selected TGO regions with a high defect density suggest that interdiffusion may proceed along microcracks through the TGO layer down to the TGO/bond coat interface.

The $CaSO_4$ pore filling did not react with the zirconia from the column walls. The reaction products from dissolution of the YSZ coating did not penetrate far into the intercolumnar gaps unless the coating has experienced tensile stresses following bond coat uplift upon rumpling.

The lack of detailed operation characteristics of the airfoil leaves the constraints of $CaSO_4$ infiltration versus CMAS deposition speculative. Condensation from a $CaSO_4$-rich vapor phase seems a reasonable proposition. On the other hand, the high water vapor partial pressure in the combustion gases may have reduced the melting temperatures of the deposits significantly. Liquid phase immiscibility between the sulfate and the silicate melt may have contributed to the layered microstructure of most $CaSO_4$/CMAS deposits.

Acknowledgements C. W. Siry, O. Schubert, and T. Fischer of Lufthansa Technik AG, Power Plant Services-Engine Parts Repair, Hamburg, Germany are gratefully acknowledged for supplying the airfoil and their continuous support. The helpful discussions with DLR colleagues U. Schulz, K. Fritscher, C. Leyens, and P. Mechnich as well as the technical assistance from R. Borath are very much appreciated.

References

1. Siry CW, Wanzek H, Dau CP (2001) Materwiss Werksttech 32:650
2. Evans AG, Mumm DR, Hutchison JW, Meier GH, Pettit FS (2001) Prog Mater Sci 46:505
3. Padture NP, Gell M, Jordan EH (2006) Science 296:280
4. Jacobson NS, Fox DS, Smialek J, Opila E, Tortorelli P, Moore F, Nickel KL, Hirata G, Yoshida M, Yuri L (2003) In: Roode MV, Ferber M, Richerson DW (eds) Ceramic gas turbine component development and characterization: progress in ceramic gas turbine development, vol 2. The American Society of Mechanical Engineers, New York, p 607
5. Stringer J (1987) Mater Sci Technol 3:482
6. Jones RL (1996) In: Stern KH (ed) Metallurgical and ceramic coatings. Chapman & Hall, London
7. Bornstein NS (1996) JOM 48:37
8. Bornstein NS, Allen WP (1997) Mater Sci Forum 251–254:127
9. Mohan P, Yuan B, Patterson T, Desai VH, Sohn YH (2007) J Am Ceram Soc 90:3601
10. Leyens C, Wright IG, Pint BA (2000) Oxid Met 54:401
11. Strangman T, Raybould D, Jameel A, Baker W (2007) Surf Coat Technol 202:658
12. Kim J, Dunn MG, Baran J, Wade DP, Tremba EL (1993) J Eng Gas Turbines Power 115:641
13. Smialek JL, Archer FA, Garlick RG (1994) JOM 139:41
14. Kräemer S, Yang J, Levi CG (2006) J Am Ceram Soc 89:3167
15. Evans AG, Clarke DR, Levi CG (2008) J Eur Ceram Soc 28:1405
16. Mercer C, Faulhaber S, Evans AG, Darolia R (2005) Acta Mater 53:1029
17. Strangman T, Neumann J, Liu A (1987) NASA, CR-179648
18. Strangman T, Schienle JL (1990) J Eng Gas Turbines Power 112:531
19. Stott FH, de Wet DJ, Taylor R (1994) MRS Bull 19(10):46
20. Borom MP, Johnson CA, Peluso LA (1996) Surf Coat Technol 87–88:116
21. Stott FH, de Wet DJ, Taylor R (1992) In: Froes FH, Wallace W, Cull RA (eds) 3rd international SAMPE metals and metals processing conference, vol 3, Advances in synthesis and processes. Stuckholt, Covinna, CA, pp 92–101
22. de Wet DJ, Stott FH (1993) J Phys IV 3(C9):655
23. Gupta DK, Duvall DS (1984) In: Gell M (ed) Superalloys 1984, TMS, Warrendale, PA, pp 711–720
24. Powder Diffraction Database PDF-2 (2000) JCPDS-ICDD: Joint Committee of Powder Diffraction Standards, International Center for Diffraction Data, Newton Square, PA
25. Taylor HFW (1997) Cement chemistry, 2nd edn. American Society of Civil Engineers, New York
26. Prince AT (1954) J Am Ceram Soc 37:402
27. Janke P (1982) Metall Mater Trans B 13:1543
28. Dravid VP, Sung CM, Notis MR, Lyman CE (1989) Acta Crystallogr B 45:218
29. Morgan PED, Hicks JL, Bump HA, Koutsoutis MS (1987) J Mater Sci Lett 6:559
30. Ito T, Sadanaga R, Takeuchi Y, Tokonami M (1969) Proc Jpn Acad 45:913
31. Braue W, Schulz U, Fritscher K, Leyens C, Wirth R (2005) Mater High Temp 22:393

32. Sohn YH, Lee EY, Nagaraj BA, Briedermann RR, Sisson RD (2001) Surf Coat Technol 146–147:132
33. Cocking JA, Burley NA, Johnston GR (1968) High Temp Technol 4:175
34. Marple BR, Voyer J, Moreau C, Nagy DR (2000) Mater High Temp 17:397
35. Du H (2000) J Phase Equilib 21:6
36. Kohl FJ, Stearns CA, Fryburg GC (1975) In: Foroulis ZA, Smeltzer FP, Marr J (eds) Metal-gas-slag reactions and processes, The Electrochemical Society, Princeton, NJ, p 649
37. Pliego-Cuervo YB, Glasser FP (1979) Cem Concr Res 9:573
38. Glasser FP, Marr J (1980) Cem Concr Res 10:753
39. Ondik HM, McMurdie HF (1998) Phase diagrams for zirconium and zirconia systems. The American Ceramic Society, Westerville
40. Pandit SS, Jacob KT (1994) Steel Res 65:410
41. Colin S, Dupre B, Venturini G, Malaman B, Gleitzer G (1993) J Solid State Chem 102:242
42. Plaisir JR, Jansen J, de Graeff RAG, Ijdo JW (1995) J Solid State Chem 115:464
43. Al-Hermezi HM, McKie D, Hall AJ (1986) Mineral Mag 50:119
44. Ansell HG, Roberts AC, Plant AG, Sturman BD (1980) Can Mineral 18:201
45. Siligardi C, Lusvarghi L, Montorsi M, Vernia C (2008) J Am Ceram Soc 91:990
46. Garcia J, Lopez T, Gomez R, Aguilar DH, Quintana P (2004) J Sol-Gel Sci Technol 32:333
47. Kraemer S, Yang J, Levi CG (2008) J Am Ceram Soc 91:576
48. Barbieri L, Cannillo V, Leonelli C, Montorsi M, Mustarelli P, Siligardi C (2003) J Phy Chem B 107:6519
49. Karell R, Chromcikowa M, Liska M (2008) Adv Mater Res 39–40:173
50. Mendis BG, Livi KJT, Hemker KJ (2006) Scripta Mater 55:649